Unwarping confocal microscopy images of bee brains by nonrigid registration to a magnetic resonance microscopy image

Torsten Rohlfing
SRI International
Neuroscience Program
333 Ravenswood Avenue
Menlo Park, California 94025
E-mail: torsten@synapse.sri.com

Frank Schaupp
Freie Universität Berlin
Institut für Biologie—Neurobiologie
Berlin, Germany

Daniel Haddad
Universität Würzburg
Physikalisches Institut EP5
Würzburg, Germany

Robert Brandt
Mercury Computer Systems GmbH
Berlin, Germany

Axel Haase
Universität Würzburg
Physikalisches Institut EP5
Würzburg, Germany

Randolf Menzel
Freie Universität Berlin
Institut für Biologie—Neurobiologie
Berlin, Germany

Calvin R. Maurer, Jr.
Stanford University
Department of Neurosurgery
Stanford, California

Abstract. Confocal microscopy (CM) is a powerful image acquisition technique that is well established in many biological applications. It provides 3-D acquisition with high spatial resolution and can acquire several different channels of complementary image information. Due to the specimen extraction and preparation process, however, the shapes of imaged objects may differ considerably from their *in vivo* appearance. Magnetic resonance microscopy (MRM) is an evolving variant of magnetic resonance imaging, which achieves microscopic resolutions using a high magnetic field and strong magnetic gradients. Compared to CM imaging, MRM allows for *in situ* imaging and is virtually free of geometrical distortions. We propose to combine the advantages of both methods by unwarping CM images using a MRM reference image. Our method incorporates a sequence of image processing operators applied to the MRM image, followed by a two-stage intensity-based registration to compute a nonrigid coordinate transformation between the CM images and the MRM image. We present results obtained using CM images from the brains of 20 honey bees and a MRM image of an *in situ* bee brain. [DOI: 10.1117/1.1896025]

Keywords: confocal microscopy imaging; magnetic resonance microscopy; nonrigid image registration; geometrical distortion.

Paper 04158 received Aug. 9, 2004; revised manuscript received Oct. 27, 2004; accepted for publication Nov. 1, 2004; published online Apr. 4, 2005.

1 Introduction

Confocal microscopy (CM) imaging is a powerful and versatile image acquisition technique that is well established in many biomedical applications.[1,2] Among its main advantages are nondestructive (at least compared to histological slicing) 3-D acquisition and high spatial resolution, which is limited mostly by the wavelength of light. Using several different fluorescent markers allows the acquisition of image data in multiple channels. Labeling and imaging of single specific neurons is also possible.[3,4]

Because of scattering and absorption of light at the wavelengths used, CM imaging is limited to thin samples, which generally means that the structure of interest needs to be exposed. Fundamentally, multiphoton microscopy, which uses pairs or triplets of infrared photons for excitation, promises increased penetration depths[5] and reduced scatter compared to single-photon CM. It is our experience, however, that in insect brains it does not currently allow penetration deeper than 200 μm through head capsule and brain (unpublished results). To obtain a 3-D image of an entire bee brain, for example, it must be removed from the head capsule. The shape of the brain as a whole and of its substructures may, therefore, be altered substantially by the time of imaging.

Magnetic resonance (MR) imaging is an imaging modality that is capable of acquiring 3-D images *in vivo* and *in situ*. While MR imaging is one of the most common imaging techniques in medical applications,[6] the spatial resolution of clinical scanners (typically 1-mm isotropic voxel size) limits its usefulness for imaging of microscopic structures. However, high-field MR spectrometers with strong magnetic field gradients that are used for microimaging can image structures on the order of magnitude of an insect brain, a process for which the term magnetic resonance microscopy (MRM) has been coined (for a review of MRM applications see Ref. 7). Using magnetic particles for contrast enhancement and labeling,

Address all correspondence to Torsten Rohlfing, Neuroscience Program, SRI International, 333 Ravenswood Avenue, BN177, Menlo Park, CA 94025-3493

1083-3668/2005/$22.00 © 2005 SPIE

structures as small as single cells have been imaged with MRM.[8–11]

Specifically in insect brains, Wecker, Hörnschemeyer, and Hoehn[12] reported resolutions of 200-μm slice thickness and 30-μm in-plane pixel size, which could be acquired in 50 min on a 7 T scanner. Jasanoff and Sun[13] achieved isotropic voxel sizes between 20 and 40 μm on a 14.1 T scanner with an acquisition time of 6 h. Haddad et al.[14] acquired data of a bee brain with a resolution of $15.6\times15.6\times30.0$ μm within 26 h using an 11.75 T magnet.

Because of the relatively lower spatial resolution, MRM cannot replace CM to image the fine details of insect brains. As an imaging modality, CM is a relatively inexpensive and high-resolution imaging technique, but it produces images with substantial geometrical distortion because of the specimen preparation process (dissection, fixation, staining, dehydration, and clearing). MRM on the other hand is a technically complex, time-consuming, and relatively low-resolution imaging technique that produces images with substantially less geometrical distortion. [Note that MR images can have geometrical distortion, due to magnetic field inhomogeneity and gradient magnitude uncertainty (scale error). These effects, however, can be minimized through the use of appropriate acquisition methods (e.g., field map corrections). They are also of substantially smaller magnitude than the effects of mechanical manipulation and chemical treatment that precede CM imaging. We address this issue in detail in Sec. 4.]

We propose to combine the advantages of both imaging modalities by using an MRM image of an insect brain as an undistorted shape reference. By computing a transformation between a CM image and an MRM image, we deform the microscopy image so that the imaged object (e.g., insect brain) matches the object imaged in MRM. If both images were acquired from the same individual, this method effectively compensates for any deformations that the specimen has undergone in preparation of the CM acquisition.

Since it is currently not logistically possible to acquire such data, we demonstrate a slightly different application of the proposed method. For the current work, the available MRM image data is from a subject that is not part of the population imaged using CM. What we achieve here is to bring all CM images into *one* common undeformed coordinate system, albeit not the one of the respective subject. The advantage of this method is that it can easily be applied to retrospective CM data, for which no corresponding MRM data is available.

Ultimately, the goal remains to develop MRM to a point where it is possible to obtain a high-resolution image for each subject that is to be imaged later using CM. In that sense, the current work is concerned with providing and evaluating the necessary basic image processing protocols and mathematical tools. From an image processing perspective, matching images from different subjects to each other, as addressed in this work, is a much harder problem than matching two images of the same subject.

2 Methods

2.1 *Confocal Microscopy Imaging*

Confocal laser scanning microscopy is a type of fluorescence microscopy where the specimen is chemically labeled with fluorescent markers. During imaging, a focused laser beam deflected by a set of xy-scanning mirrors excites the fluorescently stained specimen (i.e., the dissected brain made transparent by histological means). The emitted fluorescence is then spatially filtered by inserting a so-called ''confocal pinhole'' into the microscope's optical path. This pinhole ensures that only light from the focal plane reaches the detector, thus enabling the formation of an image that can be considered an optical section through the specimen. By moving the position of the specimen along the optical axis of the microscope, a 3-D image is generated.[1,2]

The staining of the bee brains used for the present work followed an adapted immunohistological protocol. Dissected and fixed brains were incubated with two primary antibodies (nc46, SYNORF1) that label synapse proteins.[15,16] Because cell bodies in insects reside separately from fibers and tracts, these antibodies bind well in regions of high synaptic densities, i.e., neuropil, but not in somata regions. A Cy3-conjugated secondary antibody [mouse antirabbit whole IgG (H+L)] sensitive to the primary antibody was subsequently used to render labeled regions fluorescent. After dehydration and clearing with methyl salicylate, which is a standard procedure to increase specimen transparency, the specimens were mounted in double-sided custom slides.

The brains were imaged with a confocal laser scanning microscope (Leica TCS 4D). The chromophor was excited with an ArKr laser (568-nm wavelength), and the fluorescence was detected using a long-pass filter (590-nm cutoff wavelength). The intensity of the fluorescence was quantized with a resolution of 8 bits. Due to the size of the dissected and embedded brain (about 2.5×1.6-mm laterally and about 0.8-mm axially), it cannot be imaged in a single scan. Therefore, we used multiple image-stack acquisition (3D-MISA) as described by Zuschratter et al.[17] The entire brain was scanned in 2×3 partially overlapping single scans, each using 512×512 pixels laterally and between 80 and 120 sections axially. The stacks were combined into a single 3-D image using custom software or a script running in Amira (Mercury Computer Systems, Inc., Boston, MA). Coordinates of the stack origins in the xy plane were recorded by the microscope and provided the relative positions needed for alignment of adjacent stacks. Because of the refractive index mismatch between the media in the optical path, images exhibit a shortening of distances in axial direction that was accounted for by a linear scaling factor of 1.6.[18] Examples of the final microscopy images from four different subjects are shown in Fig. 1.

2.2 *Magnetic Resonance Microscopy*

The MRM acquisition was performed on a Bruker AMX 500 spectrometer with 11.75 T and maximum gradient strength of 0.66 T/m. The solenoid coil had a length of 5.5 mm and an inner diameter of 4 mm. A constant coil and sample temperature of 5 °C was maintained during the experiment. The cooling unit utilizes a heater and temperature sensor that already exist on the AMX 500 spectrometer. Liquid nitrogen is evaporated at a constant rate and heated subsequently to keep the sample at 5 °C, which is monitored and controlled by the temperature sensor.

A 3-D spin-echo image with $256\times256\times30$ voxels, a field of view of $4.0\times4.0\times0.9$ mm, and a nominal resolution of $15.6\times15.6\times30.0$ μm was acquired. The echo time was 14.8

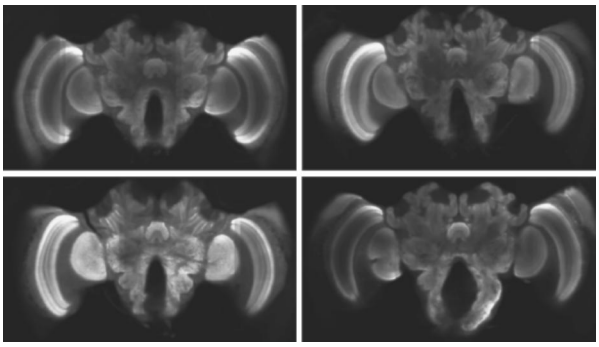

Fig. 1 Examples of CM images of bee brains. The bee brains are labeled fluorescently (see text for details). Shown are the central axial slices of the 3-D image stacks acquired from four subjects.

ms; the repetition time was 1.5 s. For the excitation, a frequency-selective pulse with a Gaussian lineshape was used, whereas for the refocusing, a nonfrequency selective block pulse was chosen. To remove DC offsets, the mean value over the last 30 points of each spin-echo acquisition was calculated and subsequently subtracted from every point of this acquisition. Zero filling by a factor of 2 prior to image reconstruction resulted in an image resolution of $7.8\times7.8\times15.0$ μm. The total acquisition time (averaging over eight repetitions) was 25.7 h. Three orthogonal slices from the resulting MRM image are shown in Fig. 2.

The preparation of the bee head reflects the tradeoff between noninvasiveness and optimization for MRM imaging contrast. To minimize the radio frequency coil's size and thus maximize its sensitivity, the head of a honey bee (Apis melifera carnica) foraging worker was separated from the thorax, and the mandibles were removed by a horizontal cut approximately 1 mm ventrally from the brain boundary. The

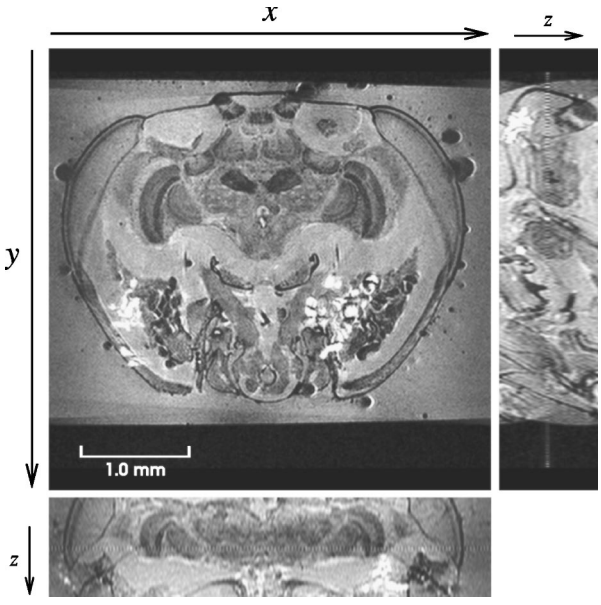

Fig. 2 An MRM image of the cranium of a honey bee. No contrast agent was used during image acquisition. Top left: axial slice. Top right: sagittal slice. Bottom left: horizontal slice. The arrows denote the three coordinate directions of the 3-D representation of this image.

tentorium, a sustaining sclerotized inner head structure ventral from the brain, was left intact, thus preventing a deformation of the head capsule. To enhance imaging contrast and to stabilize the brain's structure, the bee head was fixed overnight in a solution of 4% formalin and 0.1% Triton X before removing the mandibles. After washing the specimen for 2 h with iso-osmotic sucrose solution, the bee head was kept in 30% ethanol, which was replaced again by iso-osmotic sucrose solution prior to the MRM acquisition. To remove gas, which is dissolved in the iso-osmotic sucrose solution and fills the tracheal air sacs surrounding the brain, the bee head was evacuated for 30 min at the beginning of the fixation, and again for 10 min just prior to the MRM acquisition. For the measurement, the head was placed in a glass tube filled with iso-osmotic sucrose solution to prevent a magnetic susceptibility difference at an air-specimen border. Further details of the MRM imaging process can be found in Haddad et al.[14] and Schaupp et al.[19]

2.3 *Image Preprocessing*

To make the registration of MRM and CM images an easier problem, we apply a series of image operators to the MRM image. Figure 3 shows the individual steps and three orthogonal slices from the resulting intermediate MRM image after each of them.

The first processing step is a cropping operation that reduces the field of view of the MRM image to exclude the majority of nonbrain parts of the bee cranium. Since the MRM image exhibits severe salt-and-pepper noise, a median filter with a 3×3 neighborhood is applied next. This nonlinear filter reduces the noise while preserving edges. The next operator is a histogram equalization of the image intensities, which enhances image contrast. This is followed by an inversion of image intensities so that the brain is represented by bright voxels, whereas the background is turned dark. The final processing step is a gamma correction with $\gamma=0.2$, which improves the separation of brain and image background.

2.4 *Image Unwarping*

Unwarping the CM images is achieved by computing an anatomically correct mathematical transformation between each microscopy image and the MRM image. This procedure is commonly referred to as image-to-image registration.[20]

For the purpose of the present work, registration is a two-stage process. In the first stage, the global relative pose of both images is estimated and modeled by an affine transformation with 9 degrees of freedom (three translations, three rotations, and three anisotropic scale factors). Using a multiresolution search strategy,[21] we find the transformation parameters that maximize the normalized mutual information (NMI) image similarity measure[22] between the two images.

The second stage estimates and models the residual nonrigid component of the transformation using an algorithm first described by Rueckert et al.[23] The transformation model is a free-form deformation (FFD), which is defined on a regular, uniform grid of control points with cubic B-spline interpolation between them. As in the affine stage, the transformation parameters are determined that optimize NMI between the

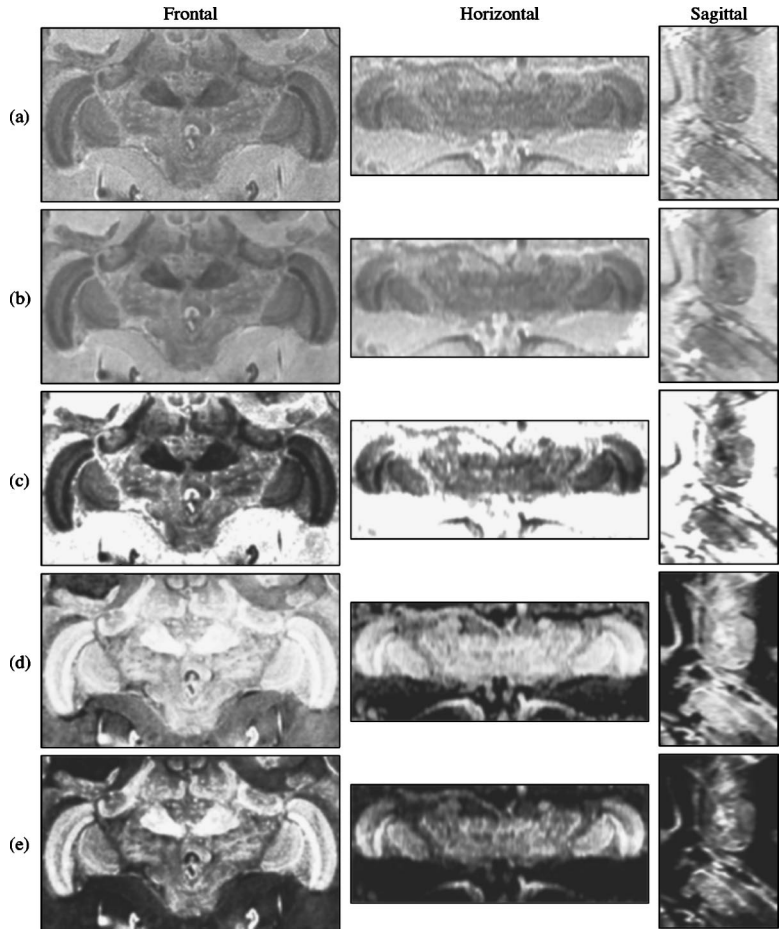

Fig. 3 Sequence of image processing operators applied to the MRM image in Fig. 2. (a) Crop field of view to approximately match microscopy image. (b) Median filter, 3×3 neighborhood. (c) Histogram equalization of image intensities. (d) Inversion of image intensities. (e) Gamma correction with γ=0.2.

two images. An efficient implementation of this algorithm with support for parallel computation keeps the computational cost within reasonable bounds.[24]

To enforce smoothness of the nonrigid coordinate transformation and to prevent unrealistic deformations and folding, we regularize the optimization function of the nonrigid registration stage. A constraint term $E_{\text{constraint}}$ is added to the NMI image similarity E_{NMI} with a user-defined weight w between zero and one. The complete optimization function is thus

$$E_{\text{total}} = (1-w)E_{\text{NMI}} - wE_{\text{constraint}}, \quad (1)$$

where the negative sign of the constraint term represents the requirement to minimize the constraint while maximizing the image similarity. In particular, we use a constraint term used by Rueckert et al.,[23] which is based on second-order derivatives of the transformation and models the bending energy of a thin metal plate.[25]

The rigid and nonrigid registration methods outlined before are only two of many successful such algorithms (for an overview of the field, see Refs. 26 and 27). We have chosen these particular methods mostly because of our own positive experience. For example, we have found the NMI image similarity measure to be relatively insensitive to noise and image intensity inhomogeneity, which is quite strong in our CM images. Likewise, the coordinate transformation model of the nonrigid registration can be substituted with a different one, but we have found the implicit smoothness constraint of the B-spline quite helpful when registering such different imaging modalities as MRM and CM.

3 Results

3.1 *Image Data and Methods*

We evaluate the proposed unwarping technique by registering CM images from 20 individuals to an MRM image from a different individual. For each subject, the CM image is independently registered to the reference MRM image, first with a 9 degrees of freedom affine transformation, followed by a nonrigid FFD transformation. Figure 4 illustrates the successive stages of alignment: rigid correction of pose and orientation differences, anisotropic scale correction, and finally, nonrigid deformation.

For the nonrigid registration, the control point spacing of the FFD was initialized as 480 μm, which in a multiresolution strategy was refined twice to reach a final resolution of 120 μm. The relatively coarse control point spacing reflects the relatively coarser resolution of the MRM image. It is also motivated by the fact that we are attempting to model defor-

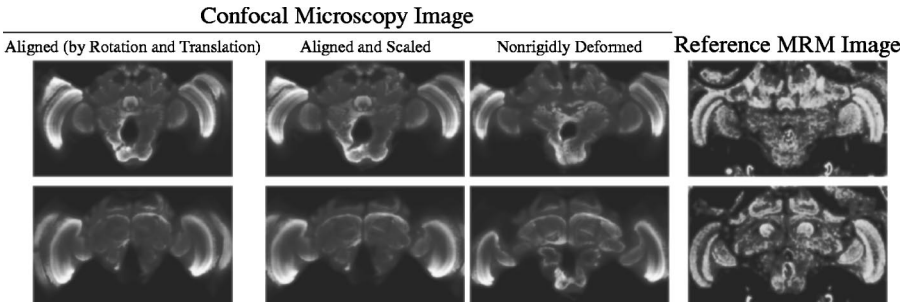

Fig. 4 Example of axial slices at two locations from the MRM image with corresponding slices from one individual CM image. The CM image is shown after alignment, scaling, and nonrigid deformation. The two slices are approximately 156 μm apart. The affine scaling factors for this subject were 1.14 in the x direction and 0.87 in the z direction (out of plane). There was no substantial scaling in the y direction.

mations of the specimen preparation process, which are likely to be smooth and coarse in scale, rather than fine-scale inter-individual shape differences. The regularization constraint weight was $w=0.01$, which we have found in previous work to produce good results.[28,29]

3.2 *Overlap Consistency of Segmented Brains*

We verify that the computed coordinate transformations between the MRM image and the CM images are meaningful by computing the overlap of manual segmentations of the brains in all images. From previous work, we have access to manual segmentations of each of the microscopy images used in the present study.[29,30] In each image, 22 anatomical structures were labeled by an expert. These segmentations are binarized to obtain a binary segmentation of the entire brain versus the image background. Similarly, we obtain a manual binary segmentation of the brain in the MRM image.

For each CM image, the binary brain segmentation is deformed according to the transformation computed between the respective CM image and the MRM image. The relative number of voxels for which both segmentations agree is a measure of how well the brains from the CM are mapped into the coordinate system of the MRM image. The results for all 20 subjects are shown in Fig. 5 (left box). The average percentage of matching voxels over all subjects is 90% with a standard deviation of 1%.

As a second experiment, we perform a leave-one-out comparison between the deformed segmented brains from the individual CM images. For that, an individual image is selected, and the remaining 19 brain segmentations are combined into an estimate of the correct segmentation.[29] Then the overlap between the selected brain and the combination of the remaining segmentations is computed. This is repeated in a round-robin manner, selecting each individual as the test case once. The results of the round-robin consistency test are also shown in Fig. 5 (right box). The average percentage of matching voxels here was 92% with a standard deviation of 2%.

3.3 *Affine Transformation Components*

The scaling factors from the affine registration are plotted by dimension in Fig. 6. It is immediately clear from this plot that the majority of the CM images are smaller in the x direction, i.e., they have a smaller lateral extent (scaling factor 0.92 $\pm$0.05, mean$\pm$standard deviation). There is also a clear increase along the z direction, i.e., in brain thickness (1.05 $\pm$0.06). The scaling factors in the y direction are tightly clustered around 1.0, i.e., on average the brains in the CM images have the same height as the one in the MRM image. The product of the three scaling factors for each subject is the total scaling factor for that subject. From Fig. 6 it appears that overall, the brain volume is smaller in the CM images than it is in the MRM image (scaling factor 0.97$\pm$0.05). In general,

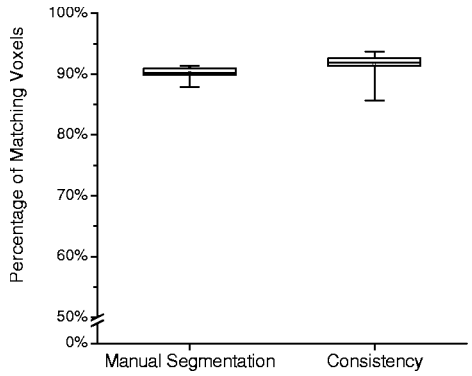

Fig. 5 Percentage of matching voxels. Left box: matching voxels between manual segmentation of brain in MRM image and coregistered CM images. Right box: matching voxels between a segmented brain in one individual deformed CM image and the consensus segmentation of the remaining deformed CM images.

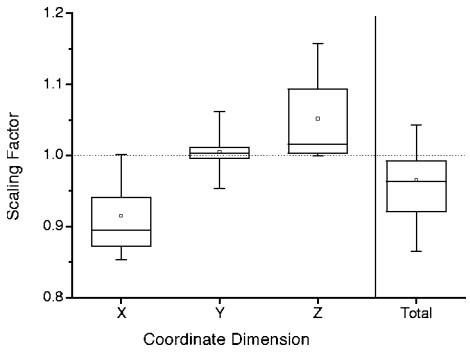

Fig. 6 Box plot of affine scaling factors by coordinate direction. The box on the far right corresponds to the total scale factor, which is the product of the individual scale factors for each subject. The scale factors are relative to the MRM image coordinates, i.e., factors smaller than one correspond to the microscopy image being smaller than the MRM image.

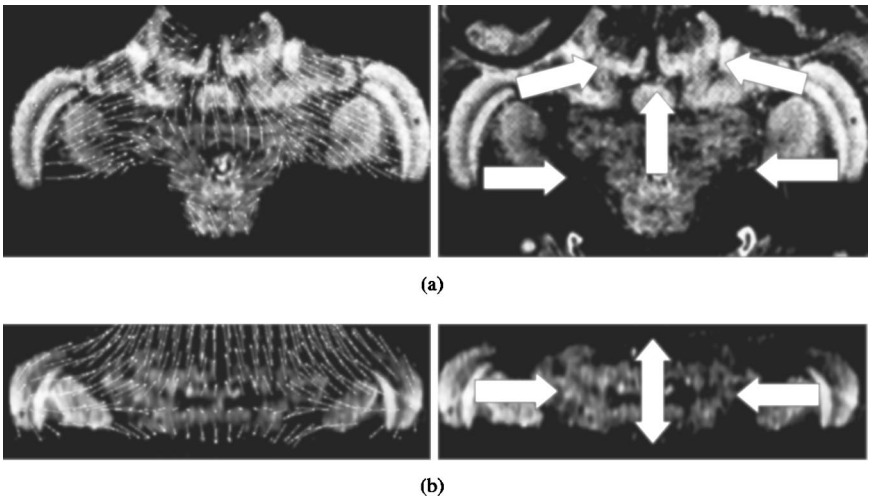

Fig. 7 Mean deformation vector field (left) and dominant deformation components (right) in MRM image coordinates. The deformation field is only shown in the brain because the deformation field in the image background outside the brain is meaningless, since it is a result of B-spline continuity and the smoothness constraint of the registration algorithm. (a) Axial slice. (b) Horizontal slice. Each arrow in the left images points in the direction of deformation; the length of an arrow represents the local deformation magnitude.

this suggests that the expansion in thickness does not entirely compensate for the lateral contraction. This is not necessarily surprising, since the bee brain is not a homogeneous block of matter, but instead an arrangement of multiple large structures with relatively small connections between them.

3.4 *Nonrigid Transformation Components*

In addition to the affine transformation components, there is substantial residual nonrigid motion. By computing the difference between affine and total motion for each image voxel, the pure nonrigid component is easily determined. To suppress the essentially random motion in the image background, we only include voxels inside the brain (as determined by manual segmentation). Averaged over all 20 subjects, the magnitude of the nonrigid motion in the brain is 94 μm. The range of the per-subject averages over all voxels is from 70 to 125 μm.

All transformations between the MRM image and the CM images are defined in the coordinate system of the MRM image. We can, therefore, easily compute the deformation field that is the mean over all microscopy images. The resulting vector field is visualized in Fig. 7. Most notable in the horizontal slice is that the shrinking in the lateral direction is accompanied by an expansion of similar magnitude along the body axis. It appears that compared to the MRM image, the brains in the microscopy images on average lost part of their width while gaining thickness. This is in good agreement with the findings of the affine analysis in the previous section. Note, however, that the scaling is not global; the expansion of the brain in the z direction, for example, is concentrated around the center of the brain, whereas the peripheral regions move inward but approximately maintain their thickness [Fig. 7(b)].

3.5 *Computational Requirements*

Although it is not one of the core points of interest for the present work, it is important to note that the methods proposed and evaluated here are computationally efficient. Memory requirements are dominated mostly by the space allocated for the image data, which is on the order of 25 to 30 MB per CM image and about 3 MB for the cropped and processed MRM image. Since we use a multiresolution pyramid of smoothed and downsampled images, and due to some storage space for the FFD control points, the total peak memory allocation is approximately 55 MB.

The image operators applied to the MRM image are easily implemented and almost instantaneous. The most expensive operator is the median filter, which takes about 2 s using a not particularly well-optimized implementation on a modern PC with a 3-GHz Intel Pentium 4 CPU (image size $290\times169\times60$ voxels). Note that the entire preprocessing needs to be applied to the MRM image only once, independent of the number of CM images to be unwarped.

Affine registration needs to be repeated for each CM image, and on average took about 25 min of computation time per subject. Nonrigid registration on average consumed about 15 min per subject. Nonrigid registration is less computationally expensive, despite the substantially larger number of degrees of freedom in the nonrigid transformation, because the B-spline interpolation functions have compact support and, therefore, each control point in the FFD only influences a small local neighborhood. This locality can be exploited for local recomputation,[24] whereas each parameter in the affine transformation has a global effect.

4 Discussion

We have demonstrated that we can successfully map CM images of bee brains onto an MRM image. Quantitative analysis of the computed transformations suggests that the preparation process preceding CM imaging leads to substantial shape changes of the specimen, most notably a lateral shrinkage of up to 15%, which is accompanied by a thickness increase of

similar magnitude. This finding is consistent with observations during specimen preparation, but can we trust our numbers?

There are several possible sources of error in the evaluation performed. To begin with, the coordinate transformation computed by the registration algorithm could simply be incorrect. To examine this possibility, we computed the overlap between a manual segmentation of the brain in the MRM image and in each of the microscopy images. We also computed the consistency of the registrations among each other in a leave-one-out fashion. Both tests showed about 90% overlap between the coregistered brains. Since we intentionally used a coarse nonrigid transformation to leave interindividual shape differences intact, this is an excellent result. Visual inspection of the deformed CM images and comparison with the MRM image further suggests that the computed coordinate transformations have high accuracy; structure boundaries in the deformed CM images align with corresponding boundaries in the MRM image substantially better than the boundaries in the original (undeformed) CM images.

The main advantage of MRM imaging is that the brain is imaged *in situ*, where it is stretched out laterally between the complex eyes, and ventrally-dorsally between the antennas and the ocelli. Leaving the brain in the head capsule with the ventral tentorium intact provides mechanical rigidity and thus minimizes brain deformation during specimen preparation. However, we have no data to support the claim that our specimen preparation for MRM imaging has no effect on brain morphology. The transformations we compute probably reflect morphological changes due to the dissection, staining, dehydration, and clearing, but might not reflect changes due to the fixation, which is common to the preparation for both imaging modalities.

The MRM image acquisition is not entirely free of geometrical distortion. First, there is scaling error in the MRM image of approximately $\pm 1.5\%$ in each coordinate direction due to error in the gradient field magnitude. This was determined by imaging a calibration phantom containing several glass capillaries with known diameters and wall thicknesses. The scaling errors are small, and they change only the size of the reference MRM image, but not its shape.

Second, there can be geometrical distortion in the MRM image due to inhomogeneities in the static magnetic field. This type of distortion occurs only in the readout gradient direction and not in phase encoding directions. We used a 3-D spin-echo image sequence with two phase encoding directions (y and z) and only one readout gradient direction (x) (Fig. 2 shows the coordinate directions). Thus any geometrical distortion due to static field inhomogeneity would occur only in the lateral (x) direction. Static field inhomogeneity can be caused by magnetic susceptibility differences between different tissues and are typically highest at air-tissue interfaces. We eliminated air-tissue interfaces by filling the tracheal air sacs surrounding the brain with iso-osmotic sucrose solution, and placing the head in a tube filled with the same solution. In our MRM image (Fig. 2), distortions due to static field inhomogeneity can be seen only at a few air bubbles near the cuticle, but not at all in the proximity of the brain. The head capsule and chitin structures, where one might expect a change in magnetic susceptibility due to trace amounts of iron, have sharp and smooth boundaries in the MRM image. Moreover, the brain in the MRM image exhibits perfect bilateral symmetry, which would have been affected by static field inhomogeneity. Thus we estimate geometrical distortion due to static field inhomogeneity to be on the order of at most 1 voxel.

Third, there can be geometrical distortion due to chemical shift. This type of distortion or artifact is observed as expected in the region of the mandibular glands (white blobs representing fat in the mandibular glands are translated horizontally to the left, leaving dark voids in the lower half of the axial slice in Fig. 2) but does not need to be considered here, because these glands are located sufficiently far from the brain itself to have any effect on the imaging of the brain, and because the lateral readout gradient direction prevents the mandibular fat signal from shifting into the brain. Because the chemical shift depends on both the applied readout gradient and the static magnetic field, the magnitude of the shift provides a check for static field inhomogeneity, at least in the areas where the chemical shift artifacts appear. The chemical shift observed in our MRM image fits the theoretical expectation very well and suggests a high static field homogeneity.

Based on these considerations, the total expected geometrical distortion in the brain in the MRM image is substantially smaller than the affine scale factors and deformation magnitudes we computed in Secs. 3.3 and 3.4.

Importantly, the subject imaged in MRM was not part of the population imaged using CM. The number of CM images is sufficiently large to capture much of the interindividual variation among different subjects. This is not the case for the single MRM image, which begs the question whether the imaged subject is a typical one or an outlier. Ultimately, we plan to image more bee brains, and in particular image the same subjects in MRM and CM. So far, this has not been logistically possible.

The question remains whether unwarping an image from one individual using an image from another individual is useful. We believe that not only is this the case, but that there are applications that require such interindividual mapping. A good example is mapping data that can only be acquired from multiple individuals, such as single-neuron images, into a common reference coordinate system. An MRM image, due to its relatively distortion-free representation of at least one individual subject, is an excellent choice to provide such a coordinate reference. Alternatively, the coordinate reference could be an average of MRM images acquired from multiple individuals.

As a final remark, we emphasize that interindividual registration of MRM and CM images is a substantially harder problem than registration of images from the same subject. With the methods in place for the former task, we are confident that we can successfully address the latter.

5 Conclusion

We present a computationally efficient methodology for unwarping CM images of insect brains by registering them to an MRM image. The proposed method includes a pipeline of image processing operations that are applied to the MRM image to support a robust and accurate registration. Preliminary results suggest that during preparation for CM imaging, the brains shrink in the lateral direction while their thickness increases. An MRM image, due to its relatively distortion-free

representation of at least one individual subject, can serve as a useful coordinate reference for mapping data that can only be acquired from multiple individuals.

Acknowledgments

R. Brandt and R. Menzel received support from the BMBF under grant numbers 0310961 and 0311558. Manual segmentations of the CM images were performed by A. Steege and C. Kaps (Freie Universität Berlin, Germany). The authors thank A. Pfefferbaum (SRI International, Menlo Park, California) for donating the computational resources needed to complete this work. We would like to thank D. Schaal (Department of Neurosurgery, Stanford University, California) for numerous comments and suggestions.

References

1. *Multidimensional Microscopy*, P. C. Cheng, T. H. Lin, W. L. Wu, and J. L. Wu, Eds., Springer-Verlag, New York (1994).
2. *Three-Dimensional Confocal Microscopy: Volume Investigation of Biological Specimens*, J. K. Stevens, L. R. Mills, and J. E. Trogadis, Eds., Academic Press, London (1994).
3. P. V. Belichenko and A. Dahlström, ''Confocal laser scanning microscopy and 3-D reconstructions of neuronal structures in human brain cortex,'' *Neuroimage* **2**(3), 201–207 (1995).
4. E. C. Marin, G. S. X. E. Jefferis, T. Komiyama, H. Zhu, and L. Luo, ''Representation of the glomerular olfactory map in the Drosophila brain,'' *Cell* **109**(2), 243–255 (2002).
5. S. G. Megason and S. E. Fraser, ''Digitizing life at the level of the cell: high-performance laser-scanning microscopy and image analysis for in toto imaging of development,'' *Mech. Dev.* **120**(11), 1407–1420 (2003).
6. R. L. Van Metter, J. Beutel, and H. L. Kundel, *Handbook of Medical Imaging, Volume 1, Physics and Psychophysics*, SPIE Press, Bellingham, WA (2000).
7. H. Benveniste and S. Blackband, ''MR microscopy and high resolution small animal MRI: applications in neuroscience research,'' *Prog. Neurobiol.* **67**(5), 393–420 (2002).
8. K. A. Hinds, J. M. Hill, E. M. Shapiro, M. O. Laukkanen, A. C. Silva, C. A. Combs, T. R. Varney, R. S. Balaban, A. P. Koretsky, and C. E. Dunbar, ''Highly efficient endosomal labeling of progenitor and stem cells with large magnetic particles allows magnetic resonance imaging of single cells,'' *Blood* **102**(3), 867–872 (2003).
9. A. C. Wright, S. L. Wehrli, G. Zhang, M. Takahashi, M. E. Hackney, D. B. Selzer, and F. W. Wehrli, ''Visualization of individual axons in excised lamprey spinal cord by magnetic resonance microscopy,'' *J. Neurosci. Methods* **114**(1), 9–15 (2002).
10. S. C. Grant, D. L. Buckley, S. Gibbs, A. G. Webb, and S. J. Blackband, ''MR microscopy of multicomponent diffusion in single neurons,'' *Magn. Reson. Med.* **46**(6), 1107–1112 (2001).
11. A. Y. Louie, M. M. Hüber, E. T. Ahrens, U. Rothbächer, R. Moats, R. E. Jacobs, S. E. Fraser, and T. J. Meade, ''In vivo visualization of gene expression using magnetic resonance imaging,'' *Nat. Biotechnol.* **18**(3), 321–325 (2000).
12. S. Wecker, T. Hörnschemeyer, and M. Hoehn, ''Investigation of insect morphology by MRI: assessment of spatial and temporal resolution,'' *J. Magn. Reson.* **20**(1), 105–111 (2002).
13. A. Jasanoff and P. Z. Sun, ''In vivo magnetic resonance microscopy of brain structure in unanesthetized flies,'' *J. Magn. Reson.* **158**(1–2), 79–85 (2002).
14. D. Haddad, F. Schaupp, R. Brandt, G. Manz, R. Menzel, and A. Haase, ''NMR imaging of the honeybee brain,'' *J. Insect Sci.* **4**, (2004). Available online: www.insectscience.org/4.7/
15. B. R. E. Klagges, G. Heimbeck, T. A. Godenschwege, A. Hofbauer, G. O. Pflugfelder, R. Reifegerste, D. Reisch, M. Schaupp, S. Buchner, and E. Buchner, ''Invertebrate synapsins: a single gene codes for several isoforms in Drosophila,'' *J. Neurosci.* **16**, 3154–3165 (1996).
16. C. Reichmuth, S. Becker, M. Benz, D. Reisch, G. Heimbeck, A. Hofbauer, B. R. E. Klagges, G. O. Pflugfelder, and E. Buchner, ''The sap47 gene of Drosophila melanogaster codes for a novel conserved neuronal protein associated with synaptic terminals,'' *Brain Res. Mol. Brain Res.* **32**, 45–54 (1995).
17. W. Zuschratter, T. Steffen, K. Braun, A. Herzog, B. Michaelis, and H. Scheich, ''Acquisition of multiple image stacks with a confocal laser scanning microscope,'' *Proc. SPIE* **3261**, 177–186 (1998).
18. D. Bucher, M. Scholz, M. Stetter, K. Obermayer, and H. J. Pflüger, ''Correction methods for three-dimensional reconstructions from confocal images: I. tissue shrinking and axial scaling,'' *J. Neurosci. Methods* **100**, 135–143 (2000).
19. F. Schaupp, ''In-situ imaging of the bee brain with NMR microscopy,'' Master's Thesis, Freie Universität Berlin, Berlin, Germany (2001).
20. D. L. G. Hill, P. G. Batchelor, M. Holden, and D. J. Hawkes, ''Medical image registration,'' *Phys. Med. Biol.* **46**, R1–R45 (2001).
21. C. Studholme, D. L. G. Hill, and D. J. Hawkes, ''Automated three-dimensional registration of magnetic resonance and positron emission tomography brain images by multiresolution optimization of voxel similarity measures,'' *Med. Phys.* **24**(1), 25–35 (1997).
22. C. Studholme, D. L. G. Hill, and D. J. Hawkes, ''An overlap invariant entropy measure of 3D medical image alignment,'' *Pattern Recogn.* **32**(1), 71–86 (1999).
23. D. Rueckert, L. I. Sonoda, C. Hayes, D. L. G. Hill, M. O. Leach, and D. J. Hawkes, ''Nonrigid registration using free-form deformations: Application to breast MR images,'' *IEEE Trans. Med. Imaging* **18**(8), 712–721 (1999).
24. T. Rohlfing and C. R. Maurer, Jr., ''Nonrigid image registration in shared-memory multiprocessor environments with application to brains, breasts, and bees,'' *IEEE Trans. Inf. Technol. Biomed.* **7**(1), 16–25 (2003).
25. G. Wahba, *Spline Models for Observational Data*, vol. 59, CBMS-NSF Regional Conf. Series, Society for Industrial and Applied Mathematics, Philadelphia, PA (1990).
26. D. Rueckert, ''Nonrigid registration: Concepts, algorithms, and applications,'' in *Medical Image Registration*, J. V. Hajnal, D. L. G. Hill, and D. J. Hawkes, Eds., pp. 281–301, CRC Press, Boca Raton, FL (2001).
27. S. K. Warfield, A. Guimond, A. Roche, A. Bharata, A. Tei, A. Talos, J. Rexilius, J. Ruiz-Alzola, C.-F. Westin, S. Haker, S. Angenent, A. Tannenbaum, F. A. Jolesz, and R. Kikinis, ''Advanced nonrigid registration algorithms for image fusion,'' in *Brain Mapping: The Methods*, 2nd ed., A. W. Toga and J. C. Mazziotta, Eds., pp. 661–690, Academic Press, San Diego (2002).
28. T. Rohlfing, C. R. Maurer, Jr., D. A. Bluemke, and M. A. Jacobs, ''Volume-preserving nonrigid registration of MR breast images using free-form deformation with an incompressibility constraint,'' *IEEE Trans. Med. Imaging* **22**(6), 730–741 (2003).
29. T. Rohlfing, R. Brandt, R. Menzel, and C. R. Maurer, Jr., ''Evaluation of atlas selection strategies for atlas-based image segmentation with application to confocal microscopy images of bee brains,'' *Neuroimage* **21**(4), 1428–1442 (2004).
30. T. Rohlfing, R. Brandt, C. R. Maurer, Jr., and R. Menzel, ''Bee brains, B-splines and computational democracy: Generating an average shape atlas,'' in *IEEE Workshop on Mathematical Methods in Biomedical Image Analysis*, L. Staib, Ed., pp. 187–194, IEEE Computer Society, Los Alamitos, CA (2001).